analytical chemistry

pubs.acs.org/ac Article

Near-Infrared Electrogenerated Chemiluminescence from Simple Copper Nanoclusters for Sensitive Alpha-Fetoprotein Sensing

Huiping Lv, Ruizhong Zhang,* Shanshan Cong, Jinna Guo, Mingzheng Shao, Wendong Liu, Libing Zhang, and Xiaoquan Lu*

Cite This: *Anal. Chem.* 2022, 94, 4538−4546 Read Online

ACCESS | Metrics & More | Article Recommendations | Supporting Information

ABSTRACT: Exploiting low cost, water-soluble, and near-infrared (NIR) emissive electrochemiluminophores (ECLphores) is significantly important for biological applications. In this study, bright and NIR electrogenerated chemiluminescence (ECL) emissive copper nanoclusters (Cu NCs) were synthesized through a facile one-pot wet chemical reduction method. ECL properties of obtained Cu NCs were examined in the presence of potassium persulfate, resulting in maximum intensity at 735 nm, at least 135 nm red-shifted with respect to all other Cu NCs. Electrochemistry, photoluminescence (PL), and spooling ECL spectroscopies were used to track NIR ECL emission of Cu NCs ascribed to the monomeric excited states. Due to the abundant binding sites of bovine serum albumin (BSA) to anchor target biomolecules, a sandwich-type ECL immunosensor was thus fabricated using such BSA-templated Cu NCs as tags and alpha fetoprotein antigen (AFP) as a model protein for the first time. Without assisting any signal amplification strategies, the proposed NIR ECL biosensor exhibited a wide linear range (1−400 ng mL^{-1}) and low detection limit (0.02 ng mL^{-1}) as well as superior selectivity and reproducibility and was successfully applied in real human serum sample determination. This work sets the stage for the development of novel non-noble metal nanoclusters for large-scale and emerging nanotechnology applications.

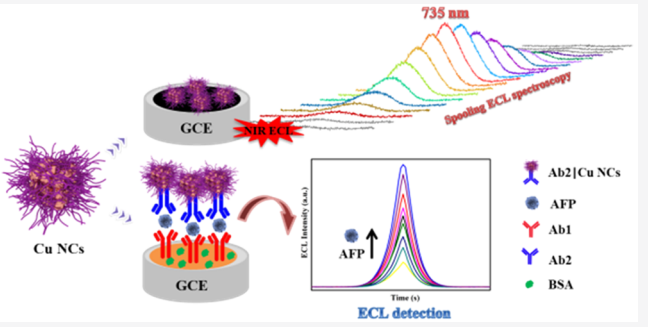

Luminophores capable of near-infrared (NIR) fluorescence are of considerable interest to the fields of material science, especially biological imaging and diagnosis. For the latter biological applications, NIR light exhibits minimal absorption by the skin and other biological tissues, which boosts light penetration and minimizes autofluorescence from biological tissues as well as reduces the photochemical damage.[1,2] Benefiting from these virtues, various NIR luminophores have been explored as labels for fluorescence sensing, imaging, and diagnosis. However, photobleaching and autofluorescence are still inevitable in NIR fluorescence bioassays because of various laser-based triggering sources for fluorescence techniques.

Compared with NIR fluorescence, NIR electrogenerated chemiluminescence has outstanding advantages such as greater tissue penetration depth, less photochemical hazard, and less background interference, which can greatly improve the detection sensitivity of target analytes.[3] Electrogenerated chemiluminescence (ECL) has been recently anticipated to be superior to fluorescence for biological applications, for example, ECL microscopy for single-cell imaging,[4,5] in terms of the absence of background from light triggers, high sensitivity for picomolar to femtomolar sensing levels, and excellent temporal and spatial controllability.[6−8] For the occurrence of ECL, highly reactive radical species must be electrogenerated in the vicinity of a biased electrode. These obtained intermediates then undergo efficient electron transfer reactions to form excited states, which relax to their ground states with emission of light. ECL can be produced through the reaction between cationic and anionic radical luminophore species generated by oxidation and reduction of a luminophore at the electrode, which is known as an annihilation pathway. Alternatively, a secondary reagent with its highly oxidative or reductive radical can be contributed to assist ECL generation, which is referred to as a coreactant route.[9−11] Due to the high redox power of these radicals derived from the secondary reagents, ECL generated via the coreactant route, is often enhanced with respect to the annihilation pathway. Electrochemiluminophores (ECLphores) are inarguably the most significant component for applications of ECL. The rapid development of nanoscience and nanotechnology affords new opportunities for exploiting nano-ECLphores except for those

Received: January 28, 2022
Accepted: February 23, 2022
Published: March 2, 2022

https://doi.org/10.1021/acs.analchem.2c00475
Anal. Chem. 2022, 94, 4538−4546

traditional organic and inorganic complexes. Due to their physicochemical properties being readily manipulated by size, composition, and surface-capping ligands, luminescent nanoparticles (semiconductor quantum dots, metal nanoclusters, *etc.*) have been widely explored as ECLphores since the first identification reported by Bard et al. in 2002.[12] Although great breakthroughs toward ECL of semiconductor quantum dots as ECLphores have been achieved, the potential toxicity from either class A elements (Cd, Hg, and Pb) or class B elements (Se and As) included in these ECLphores is a subject of serious concern for biological applications. On the basis of these concerns, metal nanoclusters stand out owing to their inherent electrochemical and photochemical features along with low toxicity and excellent biocompatibility. Importantly, Ding and co-workers have performed advanced ECL investigations on gold nanoclusters (Au NCs), in which highly efficient ECL emission in the NIR region was observed with unprecedented ECL efficiency as high as 3.5-, 5.5-, and 270-fold stronger than that of standard $Ru(bpy)_3^{2+}$ from Au_{38} NCs,[13] Au_{18} NCs,[14] and Au_{21} NCs,[15] respectively. In another recent work, Chen et al.[16] found very intense NIR ECL generated from a novel rod-shaped bimetal $Au_{12}Ag_{13}$ NCs, exhibiting a tripropylamine coreactant ECL that is 400 times higher than that of the $Ru(bpy)_3^{2+}$ reference. Although these are splendid ECL performances from Au NCs and their hybrids, the water insolubility and high cost of them for biological sensing purposes are still very challenging. Therefore, nanoclusters with near-infrared emission and excellent biocompatibility have attracted continuous attention in the field of biosensing and imaging.

In recent years, alternatively, copper nanoclusters (Cu NCs) began to attract increasing interest, not only due to their high yield under mild synthetic conditions but also because of the abundance and low cost of copper along with the excellent water solubility and biocompatibility of most Cu NCs, which shows potency for ECL applications, especially for future important biological targets. Liu et al.[17] found a red ECL emission from the dithiothreitol protected Cu NCs with a maximum emission wavelength of 600 nm, showing a superior ECL performance for Hg^{2+} detection. Yuan's group explored blue ECL emissive Cu NCs and constructed ECL biosensing platforms for sensitive determination of dopamine and microRNA.[18−20] More recently, Zhuo et al.[21] smartly confined Cu NCs in a porous poly-L-cysteine through *in situ* electrochemical reduction. They found that these confined Cu NCs showed not only much more enhanced ECL emission (at 596 nm) intensity relative to those confined-free ones but also highly sensitive ECL detection performance for alkaline phosphatase. Despite those advances, efforts devoted to exploiting the long-wavelength (like NIR region) ECL emissive Cu NCs in biological theranostics are still imperative.

Herein, bright and NIR ECL emissive Cu NCs were synthesized via a one-pot wet chemical reduction method. Photoluminescence and spooling ECL spectroscopies were used to track NIR ECL emission at 735 nm ascribed to the monomeric excited states of Cu NCs. Due to the abundant binding sites of BSA to anchor target biomolecules, such BSA-templated Cu NCs showed great promise as ECL labels for sensitive detection of alpha fetoprotein antigen with a wide linear range of 1−400 ng mL^{-1} and low detection limit of 0.02 ng mL^{-1} without assisting any signal amplification procedures.

EXPERIMENTAL SECTION

Materials and Reagents. Bovine serum albumin (BSA) was purchased from Energy Chemical (Shanghai, China) of Sun Chemical Technology Co. Ltd. Copper sulfate ($CuSO_4$, 99%), hydrazine hydrate ($N_2H_4{\cdot}H_2O$, 98%), sodium hydroxide (NaOH, 96%), dipotassium hydrogen phosphate trihydrate ($K_2HPO_4{\cdot}3H_2O$, 99%), potassium phosphate monobasic (KH_2PO_4, 99%), and potassium chloride (KCl, 99.5%) were obtained from Aladdin (Shanghai, China). Chloroauric acid hydrate ($HAuCl_4{\cdot}3H_2O$, 99.9%) was received from Meryer (Shanghai, China). Alpha fetoprotein antigen (AFP, Ag), capture AFP antibody (Ab1), detection AFP antibody (Ab2), carcinoembryonic antigen (CEA, Ag), and carcinoma antigen 19−9 (CA19−9, Ag) were bought from Linc-Bio Science Co. Ltd. (Shanghai, China). All reagents were analytical grade and used as received without further purification. Milli Q ultrapure water (18.2 MΩ cm) was used throughout all of the experiments.

Apparatus and Characterization. The transmission electron microscopy (TEM) was performed on a Tecnai G2 F20 transmission electron microscope at an accelerating voltage of 200 kV (FEI, Holland). X-ray photoelectron spectroscopy (XPS) analyses were operated with an ESCALAB-250Xi spectrometer (Thermo, UK) using an Al Kα X-ray (0.43 eV) as the light source. Ultraviolet−visible (UV−vis) absorption spectra were carried out on a UV−vis−NIR spectrophotometer (UV-3600 Plus, Shimadzu, Japan). The PL spectra and the PL decay curve were recorded on a FS05 steady-state transient fluorescence spectrometer (Thermo Field, U.S.A.) with excitation and emission slit widths set to 5 nm. A quartz cuvette with a path length of 10 mm was used for UV−vis and photoluminescence experiments. Fourier infrared (FTIR) spectra were recorded on a Nicolet is5 FTIR spectrometer (Thermo, USA) with KBr pellets.

Electrochemistry and ECL Tests. For electrochemistry and ECL measurements, a three-electrode system including a glassy carbon electrode (GCE, 3 mm in diameter), Ag/AgCl (sat. KCl), and a Pt wire served as the working electrode, reference electrode, and counter electrode, respectively. Prior to each experiment, the customized quartz cell was successively cleaned in a base bath (5% KOH, isopropanol) and an acid bath (5% HCl aqueous solution) for 4 h to prevent any contamination. The GCE working electrode was sequentially polished using 1, 0.3, and 0.05 μm alumina slurries until a mirror-like surface finished, and then it was tested with 1 mM potassium ferricyanide containing a 0.2 M KNO_3 solution until the potential difference between the cathodic peak and corresponding anodic peak of $[Fe(CN)_6]^{3-}/[Fe(CN)_6]^{4-}$ was less than 90 mV. For fabrication of the Cu NCs modified working electrode, the Cu NCs ink was first prepared by dissolving 5 mg of Cu NCs powders into 1 mL of ultrapure water under sonication; 2.5 μL of Cu NCs ink was then casted onto the surface of freshly polished GCE with a mass loading of 12.5 μg and left drying under ambient conditions. Afterward, the Cu NCs layer was coated with a thin layer of Nafion solution (0.05% in ethanol, 5 μL) to fix the Cu NCs layer firmly onto the GCE surface during the electrochemical measurements. A 0.1 M phosphate buffer solution (PBS, pH = 7.4) with 0.1 M KCl was employed as the electrolyte, which was purged with N_2 to eliminate the possible quenching effect from dissolved O_2 before each electrochemical experiment.

https://doi.org/10.1021/acs.analchem.2c00475
Anal. Chem. 2022, 94, 4538−4546

Scheme 1. Schematic Illustration of the Fabrication Procedures of the Proposed ECL AFP Immunosensor

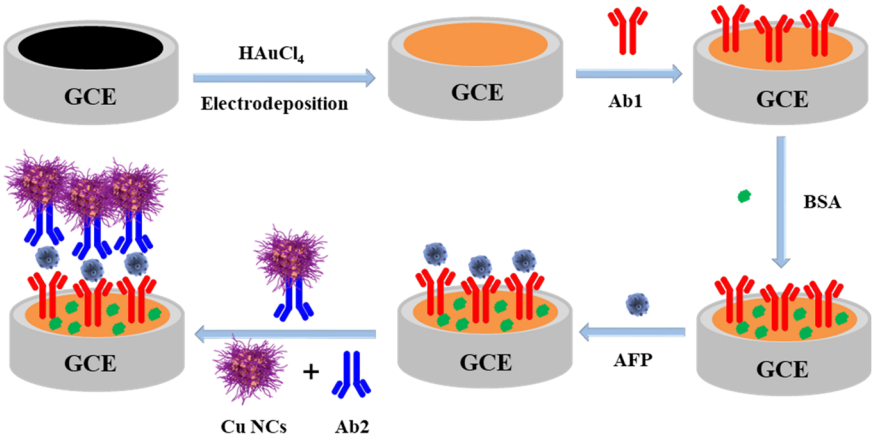

Electrochemical experiments were performed using a CHI 760E electrochemical workstation (Chenhua Instruments, Shanghai, China). Voltammetric ECL curves were recorded by correlating the applied potential to the ECL intensity from an MPI-E II ECL analyzer (Xi'an Remex Analytical Instrument Co., Ltd., China) with a photomultiplier tube (PMT) biased at 1000 V. ECL spectra were collected using an Electrogenerated Chemiluminescence Spectrum System (Model ECLS-ML, FORTEC Technology (HK) Co. Ltd., Hong Kong, China) united with a CHI 760E electrochemical workstation. Wavelength calibration was carried out by a mercury−argon lamp (Wyoptics, HG-1). The exposure time and the number of kinetic series during spooling ECL spectroscopy experiments were optimized for obtaining the clearest spectrum. And the obtained spectra were spooled together in a plot using graphing and analysis software of Origin.

Preparation of NIR ECL Emissive Cu NCs. The NIR ECL emissive Cu NCs were prepared according to reported protocols with minor modification.[22,23] In brief, 5 mL of 5 mM $CuSO_4$ aqueous solution was first prepared in a 20 mL vial; 100 mg of BSA was then added into the solution. The solution turned into a pale blue hydrogel after vigorous stirring for 10 min at room temperature. This experimental phenomenon indicates the close coordination between Cu^{2+} and various functional groups (−NH, −OH, −SH, etc.) on BSA. The pH of the hydrogel was subsequently adjusted to 12 by injecting the requisite amount of 1 M NaOH solution. In the process of the alkali condition, the pale blue hydrogel changed to a transparent purple solution within 1 min. Finally, 1 mL of hydrazine hydrate was slowly injected into the above purple solution, and the solution color turned a brownish yellow with stirring for 4 h at room temperature, suggesting the formation of Cu NCs. The obtained solution was further dialyzed for 24 h to remove small molecular impurities. A cellulose dialysis bag (MWCO: 500−1000 Da) and ultrapure Milli Q water were used, which were replaced six times over a 4 h period. The purified solution was subjected to lyophilization to remove water and to obtain a fluffy powdered form of Cu NCs.

Preparation and Fabrication Procedures of the Cu NCs-based ECL Immunosensor. As illustrated in Scheme 1, the proposed Cu NCs-based ECL analysis was fabricated in a surface-confined sandwich-type immunocomplex on GCE via a previously reported routine with minor modification.[24−26] The Cu NCs tagged as secondary AFP antibodies (Ab2-Cu NCs) were first prepared, in which 10 mg of Cu NCs was dispersed in 1 mL of 0.1 M PBS (pH = 7.4) under sonication for 15 min; 50 μL of 1 mg mL^{-1} Ab2 was then injected into Cu NC solution and further incubated at 4 °C for 5 h. It is noticeable that no additional BSA blocking procedure was employed here due to the Cu NCs in this work being capped with BSA. The obtained Ab2-Cu NCs conjugates were stored at 4 °C for further use.

The freshly polished and tested GCE was subjected to coating a layer of Au nanoparticles (Au NPs) to obtain GCE|Au NPs via potentiostatic electrodeposition at −0.2 V for 200 s by using 6 mM chloroauric acid hydrate in 0.1 M PBS (pH = 7.4) containing 0.1 M KCl as an electrolyte.[26] A total of 10 μL of 18 μg mL^{-1} of AFP primary antibody (Ab1) was subsequently dropped onto the surface of GCE|Au NPs and kept at 4 °C for 12 h to bind Ab1 through the Au−S bond. The obtained GCE|Au NPs|Ab1 was rinsed with 0.1 M PBS (pH = 7.4) to remove physically absorbed Ab1 and then blocked possible active sites on Au NPs layer with 10 μL of BSA (3%) solution at 37 °C for 1 h. A target AFP sample of various concentrations was then casted on GCE|Au NPs|Ab1 and incubated at 37 °C for 2 h to form GCE|Au NPs|Ab1|AFP conjugates via antigen−antibody specific combination interaction. The resultant electrode was finally allowed to react with 10 μL of Ab2-Cu NCs conjugates of PBS solution (0.1 M, pH = 7.4) at 37 °C for 2 h to form a GCE|Au NPs|Ab1|AFP|Ab2-Cu NCs sandwich immunosensor. Electrodes employed for selectivity experiments were fabricated in an analogous pattern without the addition of a specific antigen. The proposed Cu NCs-based ECL immunoassay was further performed in 0.1 M PBS (pH = 7.4) with 0.1 M KCl as the supporting electrolyte and 0.1 M $K_2S_2O_8$ as a coreactant at a scan rate of 400 mV s^{-1} in an optimized potential window of 0 to −1.6 V.

Synthesis and Structural Characterization of NIR ECL Emissive Cu NCs. In this study, a green one-pot wet chemical reduction method was employed to synthesize the NIR ECL emissive Cu NCs (see the Experimental Section for details). The morphology and size of Cu NCs were first studied by TEM. Figure 1A presents the low-magnification TEM image of Cu NCs dispersed in water. It can be clearly seen that the formed Cu NCs are spherical dots that are uniformly dispersed. About 100 Cu NCs were randomly selected to measure the dot size, and from the size distribution histogram shown in Figure 1A inset (bottom-right), the as-synthesized Cu NCs exhibit an average size around 1.7 nm. The high-resolution TEM image (top-right inset, Figure 1A) shows that

https://doi.org/10.1021/acs.analchem.2c00475
Anal. Chem. 2022, 94, 4538−4546

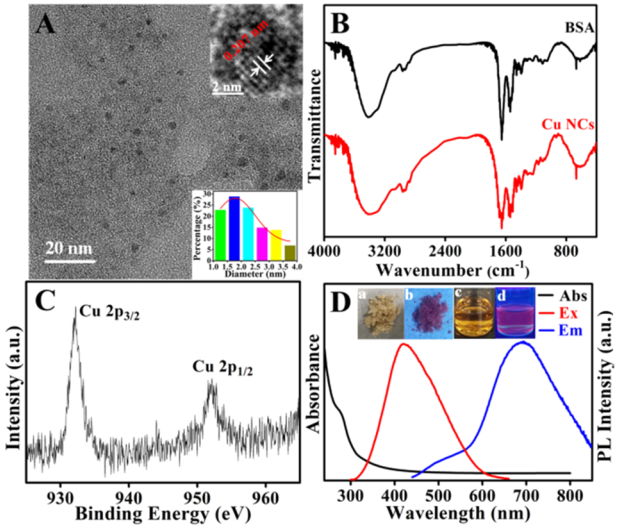

Figure 1. (A) Low-resolution TEM image of the as-synthesized Cu NCs. The insets of A display the high-resolution TEM image (top-right) and the size distribution histogram (bottom-right) of Cu NCs. (B) The FTIR spectra of the free BSA ligand and BSA capped Cu NCs. (C) High-resolution XPS spectrum of Cu 2p in Cu NCs. (D) UV−vis absorption (black), PL excitation (red), and emission (blue) spectra of the Cu NCs. The insets show the photographs of Cu NCs powder (a and b) and aqueous solution (c and d) under illumination of daylight (a and c) and UV light (365 nm, b and d).

the Cu NCs have a clearly defined fringed structure with a lattice spacing of 0.207 nm, which corresponds well to the (111) lattice planes of face-centered cubic metallic copper (JCPDS 89−2838).[21] The surface chemistry of Cu NCs was investigated by FTIR spectroscopy. Figure 1B displays the FTIR spectra of the BSA ligand and the BSA-templated Cu NCs. It is noticed from Figure 1B that the FTIR absorption characteristics from both the BSA ligand and BSA-templated Cu NCs are quite similar, indicating Cu clusters embedded inside and had been successfully protected by external BSA ligands. Due to this efficient protecting and capping effect from BSA, the obtained Cu NCs exhibit excellent uniformity with small size rather than aggregating into big nanoparticles.

X-ray photoelectron spectroscopy (XPS) was further employed to identify the composition and elemental valence states of Cu NCs. As demonstrated from the survey spectrum in Figure S1, Cu NCs are composed of all expected elements including Cu, C, N, S, O, and Na. Figure 1C displays the high-resolution XPS spectrum of Cu 2p. Two characteristic peaks located at 932 and 952 eV can be obviously observed, which are attributable to the binding energy of Cu $2p_{3/2}$ and Cu $2p_{1/2}$ electrons of metallic copper [i.e., Cu (0)]. It is worth noting that there is no prominent satellite peak at ∼942 eV, implying the absence of Cu(II) in the as-synthesized Cu NCs. Nevertheless, it is known that the binding energy difference of $2p_{3/2}$ between Cu (0) and Cu (I) is only ∼0.1 eV; therefore the valence state of the obtained Cu NCs most likely locates between 0 and +1.[27,28] The high-resolution XPS spectra of other elements are shown in the Supporting Information, Figure S2.

Optical Properties of Cu NCs. Owing to the loss of their metallic nature ascribed to the quantum confinement effect, metal nanoclusters display molecular-like electronic energy features and multiband stepwise optical absorption behavior instead of the surface plasmon resonance (SPR) band observed with larger nanoparticles. Figure 1D exhibits the UV−vis absorption profile (black curve) of Cu NCs dispersed in water. There is strong absorption in the UV region, which is attributed to the interband and intraband electronic transitions of Cu NCs because of their discrete energy levels. Note that such an optical feature is obviously disparate from the characteristic SPR band of large Cu nanoparticles at 560−600 nm.[28−30] Moreover, due to these interband transitions and intraband HOMO−LUMO transitions, metal nanoclusters exhibit well-known PL character. Notably, the aqueous solution of Cu NCs is brownish yellow under ambient daylight but shows an intense red color upon irradiation with a 365 nm UV lamp, as presented in the optical photographs in Figure 1D (insets c and d). In addition, a strong red color was also observed from Cu NCs solid powders when irradiated with a UV lamp (insets a and b of Figure 1D), in sharp contrast to its yellowish white color under daylight. Figure 1D also depicts the PL spectra of the Cu NCs. Under excitation at 422 nm (red curve), weak green and strong red luminescence with emission maxima at 505 and 690 nm can be clearly observed (blue curve), corresponding to an absolute PL quantum yield of about 1.35% at room temperature, and the calculation method of the absolute quantum yield is detailed in Supporting Information eq S1. The PL decay curve of the Cu NCs aqueous solution is shown in Figure S3, Supporting Information, which was fitted by an exponential decay profile on the basis of the nonlinear least-squares method. It can be found that the fluorescence lifetime of obtained Cu NCs at 690 nm is determined to be 15.3 ns, which resulted from the singlet excited state of Cu NCs.[31,32]

The ECL of Cu NCs was investigated next. The electrochemistry was conducted by using Cu NCs modified GCE in 0.1 M PBS (pH = 7.4) containing 0.1 M KCl, to correlate redox properties with the Cu NCs electronic structure. The differential pulse voltammograms (DPVs) in the cathodic scan demonstrated in the inset of Figure 2A exhibits one *quasi*-reversible peak at −1.38 V that resulted in a pronounced reduction current. However, in the anodic scan, no obvious oxidation peaks can be identified.

Figure 2A displays the voltammetric ECL curve for Cu NCs in the annihilation pathway. No appreciable ECL signal (blue curve) was detectable; this was expected because the Cu NCs cation radicals could not be electrogenerated in the studied solvent (as demonstrated from DPVs in Figure 2A inset) and thus there will be no annihilation reaction occurring between the Cu NCs anion radical and its radical partner. Considering the availability of anion radicals of Cu NCs demonstrated from its electrochemistry and high solubility of $K_2S_2O_8$ in aqueous solutions, we therefore explored the Cu NCs/$K_2S_2O_8$ coreactant system to see if the ECL could be enhanced. Figure 2B shows the voltammetric ECL curves of Cu NCs modified GCE with 0.1 M $K_2S_2O_8$ in 0.1 M PBS (pH = 7.4) containing 0.1 M KCl. Electrochemical reduction of $K_2S_2O_8$ with $E^{0\prime}$ of −1.38 V (red curve, Figure 2B) forms persulfate radical anion ($S_2O_8^{3-\bullet}$, eq 1) that decomposes to generate a highly reactive sulfate radical anion ($SO_4^{-\bullet}$, eq 2) with strong oxidation powder of around 2.0 V[33,34] that removes an electron from the HOMO of the Cu NCs radical anion (eq 4) that electro-reduced simultaneously from Cu NCs (Cu NCs$^{-\bullet}$, eq 3) and produces an excited state (Cu NCs*) emitting ECL (eq 5). Noticeably, the ECL onset potential (−1.15 V, blue curve) in Figure 2B is in good accordance with the onset reduction potential of Cu NCs in the DPVs (−1.10 V, inset of Figure

https://doi.org/10.1021/acs.analchem.2c00475
Anal. Chem. 2022, 94, 4538−4546

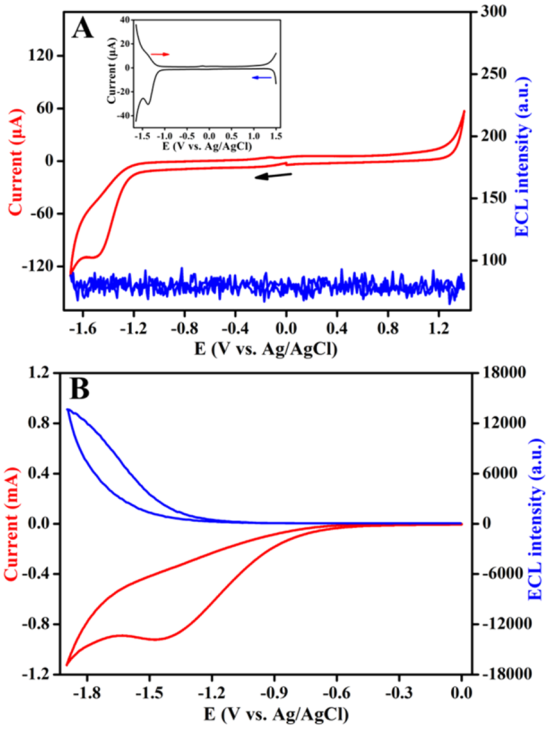

Figure 2. Cyclic voltammogram and the corresponding ECL−potential curve of Cu NCs modified GCE in the (A) absence and (B) presence of 0.1 M $K_2S_2O_8$ in 0.1 M PBS (pH = 7.4) containing 0.1 M KCl at a scan rate of 100 mV s^{-1}. The insets of differential pulse voltammetry (DPV) of Cu NCs modified GCE in 5 mL of PBS (pH = 7.4) solution, containing 0.1 M KCl.

2A). It is also found that the ECL intensity of Cu NCs first increases and then decreases with increasing the mass loading of Cu NCs on the surface of GCE (Figure S4, Supporting Information). This is because a lesser amount of Cu $NCs^{-\bullet}$ could be generated at a small mass loading and thus give a low ECL intensity. However, high mass loading would provide a thick Cu NCs modification layer on GCE that could increase the mass and electron transfer resistance, playing an infaust effect on the efficient reduction of Cu NCs for accumulation of radicals. The mass loading of 12.5 μg provides the best compromise between the radical concentration and electron/mass transfer efficiency and thus was employed in ECL measurements as proven to be its largest ECL intensity (Figure S4, Supporting Information). The ECL efficiency of the Cu NCs/$K_2S_2O_8$ coreactant system was calculated relative to the Ru(bpy)$_3$Cl$_2$/$K_2S_2O_8$ standard based on the ratio of the number of injected electrons to the number of generated photons. According to eq S2, the relative ECL efficiency of Cu NCs/$K_2S_2O_8$ (100 mM) was determined to be 50.2%.

$$S_2O_8^{2-} + e^- \rightarrow S_2O_8^{3-\bullet} \quad (1)$$

$$S_2O_8^{3-\bullet} \rightarrow SO_4^{2-} + SO_4^{-\bullet} \quad (2)$$

$$CuNCs + e^- \rightarrow CuNCs^{-\bullet} \quad (3)$$

$$CuNCs^{-\bullet} + SO_4^{-\bullet} \rightarrow CuNCs^* + SO_4^{2} \quad (4)$$

$$CuNCs^* \rightarrow CuNCs + h\nu \quad (5)$$

To gain further insight into the Cu NCs/$K_2S_2O_8$ ECL emission mechanisms, spooling ECL spectroscopy was employed to *in situ* monitor the ECL evolution, devolution, and emission peak wavelength during a potential scanning cycle. Figure 3A describes spooling ECL spectra of the Cu NCs/$K_2S_2O_8$ coreactant system during a potential sweeping from 0 V to −1.8 V and back to 0 V. The onset spooling ECL spectrum was observed at −1.10 V, with an emission peak intensity of 3754 cps at 780 nm, in red in Figure 3A. At this potential, Cu $NC^{-\bullet}$ (onset reduction potential at −1.10 V, inset of Figure 2A) begins to produce and immediately reacts with $SO_4^{-\bullet}$ (onset and peak reduction potentials at −0.69 V and −1.38 V, respectively, red line in Figure 2B), and Cu NCs* is generated. This onset potential is also in good agreement with that on the ECL-potential curve shown in Figure 2B. When the potential is swept toward more negative values, concentrations of both Cu $NCs^{-\bullet}$ and $SO_4^{-\bullet}$ in the vicinity of the electrode boost, which increases the concentration of Cu NCs* and results in ECL evolution (Figure 3B). The ECL emission reached the maximum intensity of 4809 cps at −1.8 V, while the ECL emission wavelength slightly blue-shifted to 735 nm. The 45 nm difference between the onset peak wavelength and the maximum intensity wavelength is probably due to the formation of different excited states of Cu NCs in the process of potential negative scanning as the valence state of the obtained Cu NCs is between 0 and +1 as demonstrated from XPS. Although it is hard to decide the exact content of Cu(0) and Cu(I) in the obtained Cu NCs, a series of similar valence-state-dependent ECL emission wavelength investigations on gold nanoclusters have been concluded by the Ding group.[15,35−37] Upon sweeping the potential further negative and backwards, the ECL intensity decreased owing to the depletion of the Cu $NCs^{-\bullet}$ and $SO_4^{-\bullet}$ species and led to the ECL devolution (Figure 3C).

Figure 3D depicts a PL spectrum of Cu NCs with a peak wavelength of 690 nm along with an accumulated ECL spectrum of the Cu NCs/$K_2S_2O_8$ coreactant system with a peak maximum at 735 nm acquired for 5 potential scanning cycles between 0 V and −1.8 V. The 45 nm red shift of the ECL spectrum with respect to that of PL is ascribed to the well-known inner-filter effect.[38] The ECL color emitted by the Cu NCs/$K_2S_2O_8$ system based on CIE color coordinates is a bright red light (0.53, 0.40) estimated from the CIE diagram in Figure 3E. This is a little different from its PL coordinate (0.16, 0.05) that corresponds to an orange color. It is also noteworthy that the ECL emission wavelength of current Cu NCs is at least 120 nm red-shifted compared to all reported Cu NCs capped with other ligands or employed in other coreactant systems.[18−21,39,40]

Feasibility and Characterization of Cu NCs-Based ECL Immunosensor for AFP Detection. In consideration of the prominent ECL performance, Cu NCs were further explored in the construction of a sensitive label-free ECL immunosensor for AFP detection. Electrochemical impedance spectroscopy (EIS) was first used for monitoring the assembly of the immunosensor step by step in 10 mM $[Fe(CN)_6]^{3-}$/$[Fe(CN)_6]^{4-}$ resistance (R_{et}). Concretely, it is obvious that the EIS of bare GCE exhibited almost a straight line (curve a), which proved that the bare GCE has a low R_{et}. After electrodeposition of a layer of Au NPs, a relatively smaller resistance of the obtained GCE|Au NPs (curve b) can be observed, which is ascribed to the superior conductivity of Au

https://doi.org/10.1021/acs.analchem.2c00475
Anal. Chem. 2022, 94, 4538−4546

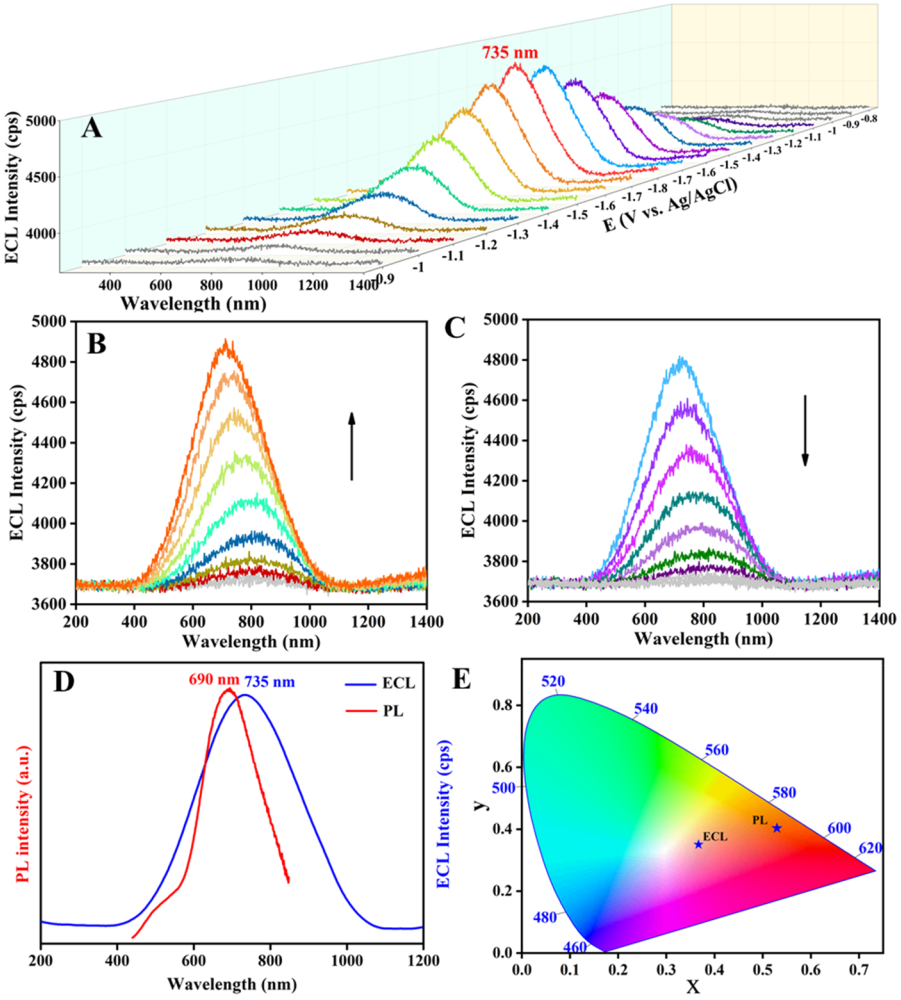

Figure 3. (A) Spooling ECL spectroscopy of Cu NC modified GCE with 0.1 M $K_2S_2O_8$ in 0.1 M PBS (pH = 7.4) containing 0.1 M KCl. The spectra were acquired at a 4 s time interval or 100 mV potential interval during potential scanning from 0 V to −1.8 V and back to 0 V at a scan rate of 25 mV s^{-1}. The potential window is shown here from −0.9 V to −1.8 V for clarity. (B, C) Stacked spooling ECL spectra for the evolution (B) and devolution (C) patterns. (D) PL spectrum of Cu NCs (red line) and accumulated ECL spectrum of Cu NCs/$K_2S_2O_8$ (blue line) in 0.1 M PBS (pH = 7.4) with 0.1 M KCl. The accumulated ECL spectrum was collected for five potential scanning cycles from 0 to −1.8 V at a scan rate of 400 mVs^{-1}. (E) The corresponding CIE color space coordinates of PL and accumulated ECL spectra of Cu NCs.

NPs, boosting the fast electron transfer of the $[Fe(CN)_6]^{3-}$/$[Fe(CN)_6]^{4-}$ redox couple. Subsequently, with the casting of Ab1 (curve c), BSA (curve d) and AFP (curve e) layer by layer, the diameter of semicircle portion increased gradually owing to the resistance of nonconductive bioactive substances that slow the electron transfer of the redox couple at the electrode surface. With the further incubation of Ab2-Cu NCs (curve f) on the electrode, the diameter of the semicircle in EIS was a little decreased. This is because the Cu NCs possess good electrical conductivity, which could enhance the electron transfer ability of the redox couple at the electrode surface. The successful assembly of the immunosensor was also confirmed by cyclic voltammetry characterization. As shown in Figure S7 Supporting Information, a dramatically increased current intensity can be seen from Au NP modified GCE (curve b) with respect to that of bare GCE (curve a), which demonstrated the excellent electrical conductivity of Au NPs and boosted the electron transfer of the $[Fe(CN)_6]^{3-}$/$[Fe(CN)_6]^{4-}$ redox pair at the electrode surface. However, the gradually decreased current intensities obviously observed after the step-by-step modification of Ab1 (curve c), BSA (curve d), AFP (curve e), and Ab2-Cu NCs (curve f) onto the GCE|Au NPs, due to the resistance of nonconductive bioactive molecules and the formation of large antibody−antigen immune complex, could slow the electron transfer of the redox probe.

Performance of the Cu NCs-Based Immunosensor for AFP Detection. The activity of immobilized antigens and antibodies could be affected by the acidity of the solution. The effect of supporting electrolyte pH on the performance of the immunosensor was investigated in the range from 6 to 8.5. As shown in Figure S5, Supporting Information, the ECL intensity of the system first increases and then decreases with increasing the pH, exhibiting the strongest ECL signal with pH = 7.4. This is due to the pH effect on the production of $SO_4^{-\bullet}$, in which $SO_4^{-\bullet}$ would be lacking under acidic conditions while $SO_4^{-\bullet}$ would be consumed by the scavenging effect of hydroxide under alkaline conditions. So neutral PBS (pH = 7.4) was used in all ECL experiments. The scan rate dependent ECL emission feature of current GCE|Au NPs|Ab1|BSA|AFP|Ab2-Cu NCs (Figure S6, Supporting Information) was observed. Under low scan rates, the GCE|Au NPs|Ab1|BSA|AFP|Ab2-Cu NCs/$K_2S_2O_8$ system exhibits lower ECL intensities likely ascribed to decreased concentrations of Cu

https://doi.org/10.1021/acs.analchem.2c00475
Anal. Chem. 2022, 94, 4538−4546

$NCs^{-\bullet}$ and $SO_4^{-\bullet}$ species as a result of decomposition that is enhanced on these longer time scales. While at higher scan rates, the radical species could be quickly accumulated and thus lead to higher ECL intensities. But the ECL intensities decrease with further increasing in scan rates from 400 mV s^{-1}, probably due to the fact that high scan rates are not conducive to hole injection of Cu NCs and oxidation of coreactants on the electrode surface.[41] Therefore, a scan rate of 400 mV s^{-1} was chosen in the following ECL immunoassay. To certify the ECL feasibility of the Cu NCs-based immunosensor, the ECL performances of various modified electrodes were first evaluated. Figure 4B exhibits the ECL-time profiles of different coated electrodes with 0.1 M $K_2S_2O_8$ in 0.1 M PBS (pH = 7.4) containing 0.1 M KCl at a scan rate of 400 mV s^{-1}. It can be seen from Figure 2B, when the bare GCE was tested, there was

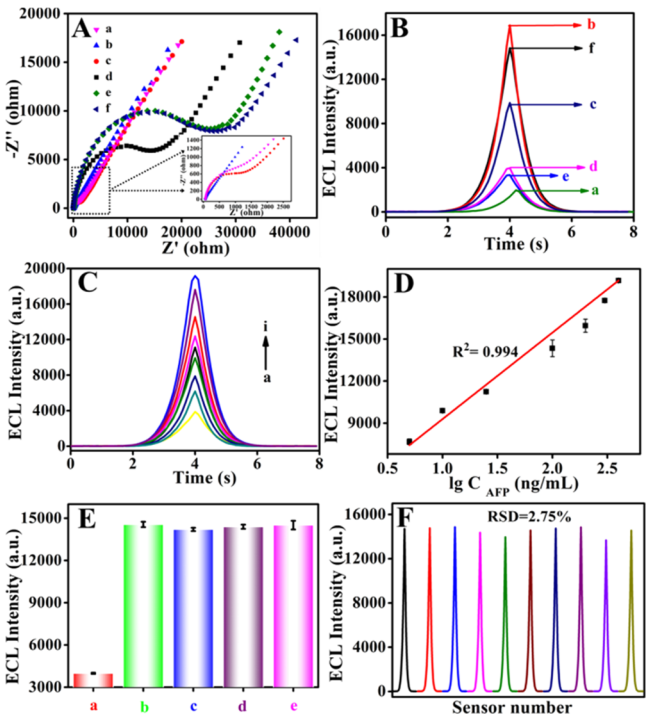

Figure 4. (A) Electrochemical impedance spectra (EIS) obtained at (a) GCE, (b) GCE|Au NPs, (c) GCE|Au NPs|Ab1, (d) GCE|Au NPs|Ab1|BSA, (e) GCE|AuNPs|Ab1|BSA|AFP, and (f) GCE|Au NPs|Ab1|BSA|AFP|Ab2-Cu NCs in the PBS (0.1 M, pH = 7.4) solution of 10 mM $[Fe(CN)_6]^{3-}/[Fe(CN)_6]^{4-}$ containing 0.1 M KNO_3. Inset of A shows the zoom-in pattern of a−c in the high frequency region. (B) ECL−time curves of studied systems with 0.1 M $K_2S_2O_8$: (a) bare GCE electrode, (b) GCE|Au NPs, (c) GCE|Au NPs|Ab1, (d) GCE|Au NPs|Ab1|BSA, (e) GCE|Au NPs|Ab1|BSA|AFP, and (f) GCE|Au NPs|Ab1|BSA|AFP|Ab2-Cu NCs. The supporting electrolyte was 0.1 M PBS containing 0.1 M KCl; the scan rate was 400 mV s^{-1}. (C) ECL−time profiles of Cu NC-based immunosensor in 0.1 M PBS/KCl (pH = 7.4) solution containing 0.1 M $K_2S_2O_8$ with various concentrations of AFP (from a to i: 0, 1.0, 5.0, 10, 25, 100, 200, 300, and 400 ng mL^{-1}, by sweeping the potential between 0 V and −1.6 V at a scan rate of 400 mV s^{-1}. (D) The corresponding calibration curve for AFP determination. (E) Selectivity of the proposed Cu NCs-based AFP biosensor: (a) blank; (b) 200 ng mL^{-1} AFP; (c) the mixture of 200 ng mL^{-1} AFP and 2 μg mL^{-1} CEA; (d) the mixture of 200 ng mL^{-1} AFP and 2 KU mL^{-1} CA19−9; (e) the mixture of 200 ng mL^{-1} AFP, 2 μg mL^{-1} CEA, and 2 KU mL^{-1} CA19−9. (F) Reproducibility and stability of the proposed Cu NCs-based immunosensor at 10 separate experiments (the concentration of AFP: 200 ng mL^{-1}).

very weak ECL signal (curve a). After the GCE was deposited with Au NPs, a remarkable ECL increase was observed (curve b), which might be due to the effectively catalytic effect of Au NPs on the ECL emission from $K_2S_2O_8$.[42,43] By contrast, as the Ab1, BSA, and AFP were coated on GCE|Au NPs in sequence (curves c−e), the ECL was significantly decreased. This is because these coated nonconductive proteins could inhibit the interfacial electron transfer. Such a result also implies that the active Au NPs could be fully covered by layer-by-layer coating of these proteins, and the ECL signal from persulfate catalyzed by Au NPs could be negligible in the fabricated immunosensor. And the role of electrodeposited Au NPs here mainly served as a carrier for immobilization of Ab1. Notably, a remarkably enhanced ECL signal was observed by further immobilization of Ab2-Cu NCs onto the electrode (curve f). This is attributable to the specific immune reactions between the AFP antibody and antigen and the efficient ECL from Cu NCs tags, all which prove the successful fabrication of a GCE|Au NPs|Ab1|BSA|AFP|Ab2-Cu NCs sandwich-type immunosensor for signal-on ECL sensing of AFP.

The proposed Cu NCs based sandwich-type immunosensor with different concentrations of AFP was then investigated. Figure 4C shows the relationship between the ECL response of the immunosensor and the incubated AFP target concentration. It is evident that ECL intensity gradually increased with increasing the concentration of AFP. As plotted in Figure 4D, an excellent linear correlation is seen between the ECL response and the logarithm of AFP concentration from 1 ng mL^{-1} to 400 ng mL^{-1}. The regression equation of the calibration curve is I_{ECL} = 6164.37 lg C_{AFP} + 3127.57 with a correlation coefficient of 0.994 (n = 5), and the limit of detection was evaluated to be as low as 0.02 ng mL^{-1} (S/N = 3). These results suggest that the proposed Cu NCs-based ECL immunosensor is highly sensitive and holds great potential in sensing AFP. Additionally, in comparison with other reported ECL tags (Table S1, Supporting Information), the current Cu NCs labels present advantages of a low cost, a low toxicity, and a much wider detection range for the determination of target AFP. Although the detection limit of the proposed immunosensor is slightly less than great, it is still fully satisfied with requirements of practical tumor patients (like C_{AFP} > 25 ng mL^{-1} for gastric cancer).

The selectivity of the proposed Cu NCs-based ECL immunosensor was further assessed. Common interfering proteins, such as CEA, CA19−9, and their mixtures, were chosen using the fabricated ECL sensor as controls. By incubating 200 ng mL^{-1} of AFP with a 100-fold higher concentration of different interfering substances, the ECL responses from AFP/interfering mixtures are almost the same as that of pure target AFP (Figure 4E), manifesting that the proposed ECL platform has excellent selectivity and specificity toward AFP. In addition, operational stability and reproducibility are vital factors to evaluate the availability of the immunosensor. As shown in Figure 4F, respective to the proposed ECL immunosensor fabricated from 10 fresh electrodes incubated with 200 ng mL^{-1} of target AFP, the ECL responses from 10 experiments show quite similar results with an RSD of only 2.75%. These results testify that the Cu NCs-based biosensor has excellent reproducibility and stability.

Real Sample Analysis. The potential application of the proposed immunosensor for practical samples was examined by detecting the AFP in serum samples. Human serum samples were provided by the School of Life Sciences, Tianjin

https://doi.org/10.1021/acs.analchem.2c00475
Anal. Chem. 2022, 94, 4538−4546

University. Fresh human serum was diluted to 100 times with 0.1 M PBS (pH 7.4) before use. As shown in Table S2, when the amount of AFP added was 10, 100, and 200 ng mL^{-1}, the average recovery rate of the immunosensor was observed in these enhanced samples in the range of 100.2−104.1% with an RSD of 1.7−2.8% (n = 3), which further shows that the manufactured immunosensor has reliable and satisfactory applications in clinical assays.

CONCLUSIONS

In conclusion, we report a low-cost and water-soluble ECLphore of Cu NCs, synthesized through a facile one-pot wet chemical reduction method and capable of NIR ECL. The obtained Cu NCs exhibit intense solution and solid-state PL with an absolute quantum yield of 1.35%. The electrochemical properties of Cu NCs were probed using cyclic voltammetry and differential pulse voltammetry, and revealed one quasi-reversible reduction within the electrochemical solvent window provided by water. No ECL was observed from Cu NCs in the annihilation route, but intense ECL was induced upon the addition of $K_2S_2O_8$ and led to maximum intensity at 735 nm, at least 135 nm red-shifted with respect to all other Cu NCs. Spooling ECL spectroscopy was used to track NIR ECL emission ascribed to the monomeric excited states. Due to the abundant binding sites of BSA to anchor target biomolecules, a sandwich-type ECL immunosensor was then constructed by using current Cu NCs as tags and AFP as a mode protein. The proposed Cu NCs-based ECL biosensor exhibited a wide linear range of 1−400 ng mL^{-1} and a low detection limit of 0.02 ng mL^{-1} as well as superior selectivity and reproducibility, without assisting any signal amplification strategies. On the basis of its high yield under mild synthetic conditions, the abundance and low cost of the precursor as well as unique properties, we envision that this work will inspire the development of novel non-noble metal nanoclusters for emerging biological applications involving NIR electrogenerated chemiluminescent nanomaterials.

ASSOCIATED CONTENT

Supporting Information

The Supporting Information is available free of charge at https://pubs.acs.org/doi/10.1021/acs.analchem.2c00475.

Extra XPS characterization data of Cu NCs; PL lifetime decay curve of Cu NCs; the relationship between ECL intensity and mass loading of Cu NCs on GCE surface; the scan rate dependent ECL intensity of the Cu NCs/$K_2S_2O_8$ coreactant system; cyclic voltammograms of the step-by-step assembly process of the Cu NCs-based immunosensor; the analytical performance comparison of current work with previously reported ones (PDF)

AUTHOR INFORMATION

Corresponding Authors

Ruizhong Zhang − *Tianjin Key Laboratory of Molecular Optoelectronic Sciences, Department of Chemistry, Tianjin University, Tianjin 300072, China*; Email: zhangrz2019@tju.edu.cn

Xiaoquan Lu − *Key Laboratory of Bioelectrochemistry and Environmental Analysis of Gansu Province, College of Chemistry and Chemical Engineering, Northwest Normal University, Lanzhou 730070, China*; orcid.org/0000-0003-2375-668X; Email: luxq@nwnu.edu.cn

Authors

Huiping Lv − *Tianjin Key Laboratory of Molecular Optoelectronic Sciences, Department of Chemistry, Tianjin University, Tianjin 300072, China*

Shanshan Cong − *Tianjin Key Laboratory of Molecular Optoelectronic Sciences, Department of Chemistry, Tianjin University, Tianjin 300072, China*

Jinna Guo − *Tianjin Key Laboratory of Molecular Optoelectronic Sciences, Department of Chemistry, Tianjin University, Tianjin 300072, China*

Mingzheng Shao − *Tianjin Key Laboratory of Molecular Optoelectronic Sciences, Department of Chemistry, Tianjin University, Tianjin 300072, China*

Wendong Liu − *Tianjin Key Laboratory of Molecular Optoelectronic Sciences, Department of Chemistry, Tianjin University, Tianjin 300072, China*

Libing Zhang − *Tianjin Key Laboratory of Molecular Optoelectronic Sciences, Department of Chemistry, Tianjin University, Tianjin 300072, China*; orcid.org/0000-0002-7983-7326

Complete contact information is available at: https://pubs.acs.org/10.1021/acs.analchem.2c00475

Notes

The authors declare no competing financial interest.

ACKNOWLEDGMENTS

The authors gratefully acknowledge the support from the National Natural Science Foundation of China (No. 22127803, 22174110, 22004089, and 21904095), the Program of Tianjin Science and Technology Major Project and Engineering (No. 19ZXYXSY00090), the Industrial Support Plan of Gansu Provincial Department of Education (No. 2021cyzc-01), the Special Fund Project for Guiding Local Scientific and Technological Development by the Central Government (No. 2020-2060503-17), and the Opening Project of Key Laboratory of Optoelectronic Chemical Materials and Devices of Ministry of Education, Jianghan University (No. JDGD-202027). The authors also thank the Young Thousand Talented Program and Peiyang Talents Project of Tianjin University for Prof. Libing Zhang.

REFERENCES

(1) Miao, Q.; Pu, K. *Adv. Mater.* **2018**, *30*, 1801778.
(2) Yu, X.; Ying, Y.; Feng, Z.; Qi, J.; Zheng, J.; Zhang, Y.; Liu, J.; Qian, J.; Tang, B. Z.; Zhang, D. *Nano Today* **2021**, *39*, 101235.
(3) Liu, J. L.; Zhang, J. Q.; Tang, Z. L.; Zhuo, Y.; Chai, Y. Q.; Yuan, R. *Chem. Sci.* **2019**, *10*, 4497−4501.
(4) Chen, Y.; Gou, X.; Ma, C.; Jiang, D.; Zhu, J.-J. *Anal. Chem.* **2021**, *93*, 7682−7689.
(5) Ma, Y.; Colin, C.; Descamps, J.; Arbault, S.; Sojic, N. *Angew. Chem., Int. Ed.* **2021**, *60*, 18742.
(6) Kurita, R.; Arai, K.; Nakamoto, K.; Kato, D.; Niwa, O. *Anal. Chem.* **2010**, *82*, 1692−1697.
(7) Kurita, R.; Arai, K.; Nakamoto, K.; Kato, D.; Niwa, O. *Anal. Chem.* **2012**, *84*, 1799−1803.
(8) Chen, Y.; Xu, J.; Su, J.; Xiang, Y.; Yuan, R.; Chai, Y. *Anal. Chem.* **2012**, *84*, 7750−7755.
(9) Richter, M. M. *Chem. Rev.* **2004**, *104*, 3003−3036.
(10) Miao, W. *Chem. Rev.* **2008**, *108*, 2506−2553.
(11) Hesari, M.; Ding, Z. J. *Electrochem. Soc.* **2016**, *163*, H3116−H3131.
(12) Ding, Z.; Quinn, B. M.; Haram, S. K.; Pell, L. E.; Korgel, B. A.; Bard, A. J. *Science* **2002**, *296*, 1293−1297.

(13) Hesari, M.; Workentin, M. S.; Ding, Z. *ACS Nano* **2014**, *8*, 8543−8553.
(14) Hesari, M.; Ding, Z. *Chem. Eur. J.* **2021**, *27*, 14821−14825.
(15) Hesari, M.; Ding, Z. *J. Am. Chem. Soc.* **2021**, *143*, 19474.
(16) Chen, S.; Ma, H.; Padelford, J. W.; Qinchen, W.; Yu, W.; Wang, S.; Zhu, M.; Wang, G. J. *Am. Chem. Soc.* **2019**, *141*, 9603−9609.
(17) Liu, H.; Gao, X.; Zhuang, X.; Tian, C.; Wang, Z.; Li, Y.; Rogach, A. L. *Analyst* **2019**, *144*, 4425−4431.
(18) Zhao, M.; Chen, A.-Y.; Huang, D.; Zhuo, Y.; Chai, Y.-Q.; Yuan, R. *Anal. Chem.* **2016**, *88*, 11527−11532.
(19) Liao, H.; Zhou, Y.; Chai, Y.; Yuan, R. *Biosens. Bioelectron.* **2018**, *114*, 10−14.
(20) Zhou, Y.; Wang, H.; Zhang, H.; Chai, Y.; Yuan, R. *Anal. Chem.* **2018**, *90*, 3543−3549.
(21) Pan, M.-C.; Lei, Y.-M.; Chai, Y.-Q.; Yuan, R.; Zhuo, Y. *Anal. Chem.* **2020**, *92*, 13581−13587.
(22) Wang, C.; Wang, C. X.; Xu, L.; Cheng, H.; Lin, Q.; Zhang, C. *Nanoscale* **2014**, *6*, 1775−1781.
(23) Li, X. G.; Zhang, F.; Gao, Y.; Zhou, Q. M.; Zhao, Y.; Li, Y.; Huo, J. Z.; Zhao, X. J. *Biosens. Bioelectron.* **2016**, *86*, 270−276.
(24) Zhou, Y.; Chen, S.; Luo, X.; Chai, Y.; Yuan, R. *Anal. Chem.* **2018**, *90*, 10024−10030.
(25) Zhang, X.; Tan, X.; Zhang, B.; Miao, W.; Zou, G. *Anal. Chem.* **2016**, *88*, 6947−6953.
(26) Song, Y.; Zhang, W.; He, S.; Shang, L.; Ma, R.; Jia, L.; Wang, H. *ACS Appl. Mater. Interfaces* **2019**, *11*, 33676−33683.
(27) Jia, X.; Li, J.; Wang, E. *small* **2013**, *9*, 3873−3879.
(28) Wei, W. T.; Lu, Y. Z.; Chen, W.; Chen, S. W. J. *Am. Chem. Soc.* **2011**, *133*, 2060−2063.
(29) Lisiecki, I.; Billoudet, F.; Pileni, M. P. J. *Phys. Chem.* **1996**, *100*, 4160−4166.
(30) Salzemann, C.; Lisiecki, I.; Brioude, A.; Urban, J.; Pileni, M. P. J. *Phys. Chem. B* **2004**, *108*, 13242−13248.
(31) Shi, Y. e.; Ma, J.; Feng, A.; Wang, Z.; Rogach, A. L. *Aggregate* **2021**, *2*, e112.
(32) Shang, L.; Dong, S.; Nienhaus, G. U. *Nano Today* **2011**, *6*, 401−418.
(33) Bolleta, F.; Ciano, M.; Balzani, V.; Serpone, N. *Inorg. Chim. Acta* **1982**, *62*, 207−213.
(34) Memming, R. *J. Electrochem. Soc.* **1969**, *116*, 785.
(35) Hesari, M.; Ding, Z. *Acc. Chem. Res.* **2017**, *50*, 218−230.
(36) Hesari, M.; Ding, Z. F. *Chem.—Eur. J.* **2021**, *27*, 14821−14825.
(37) Yu, L.; Zhang, Q.; Kang, Q.; Zhang, B.; Shen, D. Z.; Zou, G. Z. *Anal. Chem.* **2020**, *92*, 7581−7587.
(38) Nepomnyashchii, A. B.; Cho, S.; Rossky, P. J.; Bard, A. J. J. *Am. Chem. Soc.* **2010**, *132*, 17550−17559.
(39) Liu, H.; Gao, X.; Zhuang, X.; Tian, C.; Wang, Z.; Li, Y.; Rogach, A. L. *Analyst* **2019**, *144*, 4425−4431.
(40) Zhuang, X.; Gao, X.; Tian, C.; Cui, D.; Luan, F.; Wang, Z.; Xiong, Y.; Chen, L. *Chem. Commun.* **2020**, *56*, 5755−5758.
(41) Liang, G.; Liu, S.; Zou, G.; Zhang, X. *Anal. Chem.* **2012**, *84*, 10645−10649.
(42) Niu, H.; Yuan, R.; Chai, Y.; Mao, L.; Liu, H.; Cao, Y. *Biosens. Bioelectron.* **2013**, *39*, 296−299.
(43) Dai, H.; Xu, G.; Zhang, S.; Gong, L.; Li, X.; Yang, C.; Lin, Y.; Chen, J.; Chen, G. *Biosens. Bioelectron.* **2014**, *61*, 575−578.

https://doi.org/10.1021/acs.analchem.2c00475
Anal. Chem. 2022, 94, 4538−4546